

PAPER • OPEN ACCESS

Cavity-enhanced spectroscopy of a few-ion ensemble in $\text{Eu}^{3+}:\text{Y}_2\text{O}_3$

To cite this article: Bernardo Casabone *et al* 2018 *New J. Phys.* **20** 095006

View the [article online](#) for updates and enhancements.



IOP | ebooks™




Bringing you innovative digital publishing with leading voices to create your essential collection of books in STEM research.

Start exploring the collection - download the first chapter of every title for free.



PAPER

Cavity-enhanced spectroscopy of a few-ion ensemble in $\text{Eu}^{3+}:\text{Y}_2\text{O}_3$

Bernardo Casabone^{1,2} , Julia Benedikter^{2,3,4}, Thomas Hümmer^{2,3}, Franziska Oehl³, Karmel de Oliveira Lima⁵, Theodor W Hänsch^{2,3}, Alban Ferrier^{5,6}, Philippe Goldner^{5,6}, Hugues de Riedmatten^{1,7}  and David Hunger ⁴

¹ ICFO-Institut de Ciències Fòniques, The Barcelona Institute of Science and Technology, 08860 Castelldefels, Barcelona, Spain

² Max-Planck-Institut für Quantenoptik, Hans-Kopfermann-Straße 1, D-85748 Garching, Germany

³ Fakultät für Physik, Ludwig-Maximilians-Universität, Schellingstraße 4, D-80799 München, Germany

⁴ Karlsruher Institut für Technologie, Physikalisches Institut, Wolfgang-Gaede-Str. 1, D-76131 Karlsruhe, Germany

⁵ Université PSL, Chimie ParisTech, CNRS, Institut de Recherche de Chimie Paris, F-75005 Paris, France

⁶ Sorbonne Université, F-75005 Paris, France

⁷ ICREA-Institució Catalana de Recerca i Estudis Avançats, E-08015 Barcelona, Spain

E-mail: david.hunger@kit.edu

Keywords: solid state quantum memories, quantum networks, fiber-based microcavity, single ion detection, europium-doped nanocrystal

RECEIVED
24 April 2018

REVISED
29 August 2018

ACCEPTED FOR PUBLICATION
6 September 2018

PUBLISHED
28 September 2018

Original content from this work may be used under the terms of the [Creative Commons Attribution 3.0 licence](https://creativecommons.org/licenses/by/4.0/).

Any further distribution of this work must maintain attribution to the author(s) and the title of the work, journal citation and DOI.



Abstract

We report on the coupling of the emission from a single europium-doped nanocrystal to a fiber-based microcavity under cryogenic conditions. As a first step, we study the properties of nanocrystals that are relevant for cavity experiments and show that embedding them in a dielectric thin film can significantly reduce scattering loss and increase the light–matter coupling strength for dopant ions. The latter is supported by the observation of a fluorescence lifetime reduction, which is explained by an increased local field strength. We then couple an isolated nanocrystal to an optical microcavity, determine its size and ion number, and perform cavity-enhanced spectroscopy by resonantly coupling a cavity mode to a selected transition. We measure the inhomogeneous linewidth of the coherent 5D_0 – 7F_0 transition and find a value that agrees with the linewidth in bulk crystals, evidencing a high crystal quality. We detect the fluorescence from an ensemble of few ions in the regime of power broadening and observe an increased fluorescence rate consistent with Purcell enhancement. The results represent an important step towards the efficient readout of single rare earth ions with excellent optical and spin coherence properties, which is promising for applications in quantum communication and distributed quantum computation.

1. Introduction

Rare earth ion-doped crystals constitute a promising solid state system for quantum information processing and networking [1]. They provide nuclear spin states with very long coherence times, up to six hours [2], in which quantum information can be stored [3–5]. They also offer $4f$ – $4f$ optical transitions with exceptionally good coherence properties, up to 4.3 ms [6], that can be used as a photonic interface for the spin states. Furthermore, electric dipole interactions can be used for an excitation blockade similar to the one studied for Rydberg atoms, and are thus a resource to realize quantum gates [7, 8]. However, due to the dipole-forbidden transitions, the excited state lifetime is long, leading to very low emission rates. This has limited most experiments to macroscopic ensembles so far, which hinders scalability towards multi-qubit systems.

Recently, individual rare earth ions have been detected either by upconversion spectroscopy [9], direct high resolution spectroscopy of $4f$ – $4f$ transitions [10, 11], or by using strong $5d$ – $4f$ transitions [3, 12]. For the realization of spin-photon interfaces, the coherent $4f$ – $4f$ transitions appear to be best suited. However, their low scattering rate makes single ion detection in free space challenging. Moreover, the excited state lifetime is typically significantly longer than the coherence time, deteriorating the indistinguishability of the emitted photons. Both issues can be overcome by coupling the emitters to optical microcavities. This increases the low scattering rates to achieve practically useful detection rates [2, 13, 14]. Coupling the emitters to optical

microcavities increases the spontaneous emission rate by the Purcell factor $C = \zeta \frac{3\lambda^3}{4\pi^2} \frac{Q}{V_m}$, where λ is the emission wavelength, Q the quality factor of the resonator, V_m its mode volume, and ζ the branching ratio of the respective transition. Additionally, the emission is coupled to a well-collectible cavity mode, yielding a collection efficiency given by $\beta = \eta C / (C + 1)$ with the cavity outcoupling efficiency η . Near-unity collection efficiency can be reached for sufficiently large C and η . Finally, for $C > 2\gamma_h\tau$, where τ is the excited state lifetime and γ_h is the homogeneous linewidth, emitted photons are Fourier limited [14–17], thus allowing for interference between photons from different ions as required for scalable entanglement distribution using entanglement swapping [18] as already shown in other systems [19, 20].

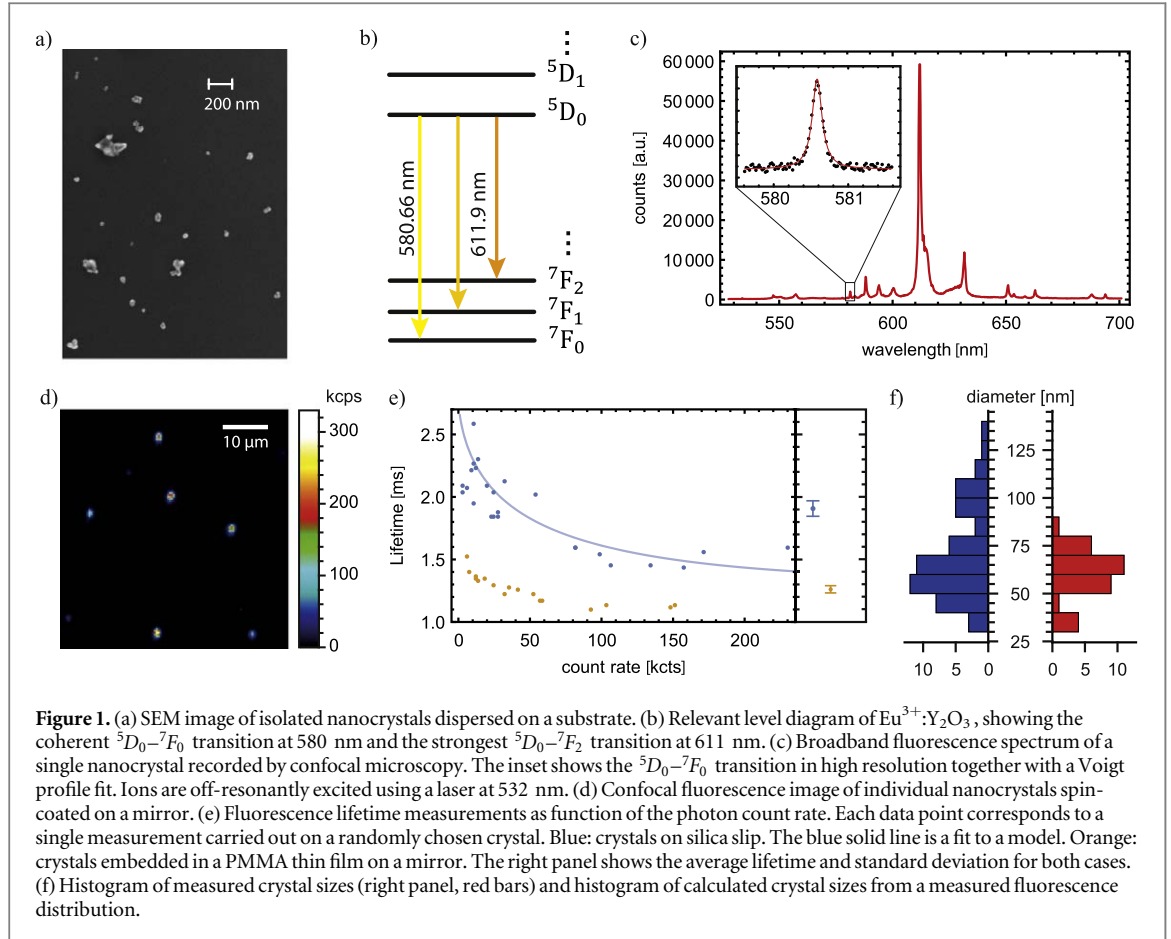
Here, we report on a promising approach for achieving efficient access to individual or small ensembles of ions by coupling ion-doped nanocrystals to a high-finesse fiber-based Fabry–Perot microcavity [21, 22]. Fiber cavities can achieve high Purcell factors up to 10^4 , provide open access to the cavity mode for optimal overlap between the ions and the cavity field, and offer full tunability of the resonance frequency to target all regions of the inhomogeneous line. We show that introducing small enough nanoparticles into the cavity does not significantly affect the cavity, and allows one to independently optimize the cavity and the sample. In particular, we demonstrate that embedding nanoparticles into a dielectric layer on a cavity mirror is beneficial for both reducing scattering loss and increasing the local field strength at the ions, significantly improving ion-cavity coupling. Nanoparticles naturally select a small ensemble of ions, such that due to a large ratio between the inhomogeneous and the homogeneous linewidth, individual ions can be addressed via their transition frequency. We study $\text{Eu}^{3+}:\text{Y}_2\text{O}_3$ nanocrystals, which to date have shown the best optical and spin coherence within a nanoscale host, with a homogeneous linewidth $\gamma_h = 45$ kHz [23, 24] and 8 ms nuclear spin coherence [25] observed in nanoparticle powders. Europium also offers a hyperfine structure that can be used to store and process quantum information [26]. We demonstrate cavity-enhanced low-temperature spectroscopy of a few-ion ensemble in a crystal where the size and thus the contained ion number is known. We estimate the achieved cavity enhancement and deduce the number of ions that contribute to the signal. The approach is promising for efficient single ion detection and could be a basis to realize quantum nodes for quantum communication and information processing.

2. Single nanocrystal fluorescence, scattering and lifetime

We investigate the properties of nanocrystals with a confocal setup (air objective with $\text{NA} = 0.9$) at room temperature to obtain reference values of optical properties and to optimize the integration of crystals into a microcavity with the aim to minimize scattering loss and maximize the light–matter coupling.

We study 0.5% $\text{Eu}^{3+}:\text{Y}_2\text{O}_3$ nanoparticles with an average size of 60 nm synthesized by homogeneous precipitation [27]. Figure 1(a) shows a scanning electron micrograph of nanocrystals dispersed on a substrate. Figure 1(d) shows a confocal fluorescence image of individual nanocrystals spin-coated on a mirror. We excite under saturation conditions (~ 1 mW, $\text{NA} = 0.9$) with 532 nm light, which is close to the ${}^5D_1 - {}^7F_1$ transition. The emission occurs from 5D_0 with several transitions into different spin–orbit ground state levels. Figure 1(b) shows a simplified scheme of the relevant levels and transitions studied here. We record spectra of individual crystals and assess the room temperature linewidth of the ${}^5D_0 - {}^7F_0$ transition, which gives a first impression of the crystal quality. Figure 1(c) shows a broadband fluorescence spectrum of a single crystal, and the inset shows the ${}^5D_0 - {}^7F_0$ transition in high resolution. Even for nanocrystals with very low count rate, which are correspondingly small and thus compatible with cavity experiments, we observe a linewidth of 80 GHz, which is as narrow as in bulk samples.

Next, we study a large number of isolated nanocrystals and infer the peak count rate per crystal. By looking at the count rate distribution and comparing with a size distribution obtained from SEM images such as the one shown in figure 1(a), we can get an order of magnitude estimate for the typical count rate per single ion. Figure 1(f) shows a histogram of the measured crystal size (red, right) and the expected crystal size distribution calculated from the measured fluorescence values (blue, left). Here we assume that the count rate R and crystal radius r are directly related via $R = NR_0 = (4\pi/3)n_0r^3R_0$, where R_0 is the single ion count rate and N the number of ions. From the size and doping concentration, and knowing that the Y concentration in the C2 site is $n_0 = 1.6 \times 10^{22} \text{ cm}^{-3}$, single crystals of e.g. 60 nm diameter contain $N \sim 10^4$ ions. The two distributions match if we assume an excited state population of 20% (several ground state levels are thermally populated, but only one is excited at about one saturation intensity) and an overall fluorescence detection efficiency of 1.5%. This value is smaller than the expected maximally achievable detection efficiency of 20% for our setup, which we calculate from the modified dipole emission pattern on a Bragg mirror averaged over dipole orientations, the angular collection efficiency of the microscope objective, the maximal transmission through the optics, and the detector quantum efficiency [22]. The smaller experimental value is ascribed to suboptimal collection and transmission efficiency and a potential overestimation of the excited state population. The analysis shows that



we detect about 2 photons per second per ion, which at best could be increased to $100 \text{ photons s}^{-1}$, rendering single ion experiments unpractical under free space conditions.

Two crucial aspects for the cavity experiment are the scattering loss introduced by the nanocrystal and the achievable ion–photon coupling strength, where the latter depends on the partially suppressed local electric field inside the crystal. Indeed, scattering loss and local field suppression both arise from the boundary condition introduced by the nanocrystal surface, and are related to modes outside or inside the crystal, respectively. In the Rayleigh regime $r \ll \lambda/2\pi$, the scattering loss

$$B = 4\sigma/\pi w_0^2 \quad (1)$$

can be calculated from the cavity mode waist w_0 and the scattering cross section

$$\sigma = \left(\frac{2\pi}{\lambda}\right)^4 \frac{\alpha^2}{6\pi}, \quad (2)$$

with the polarizability of the crystal [28]

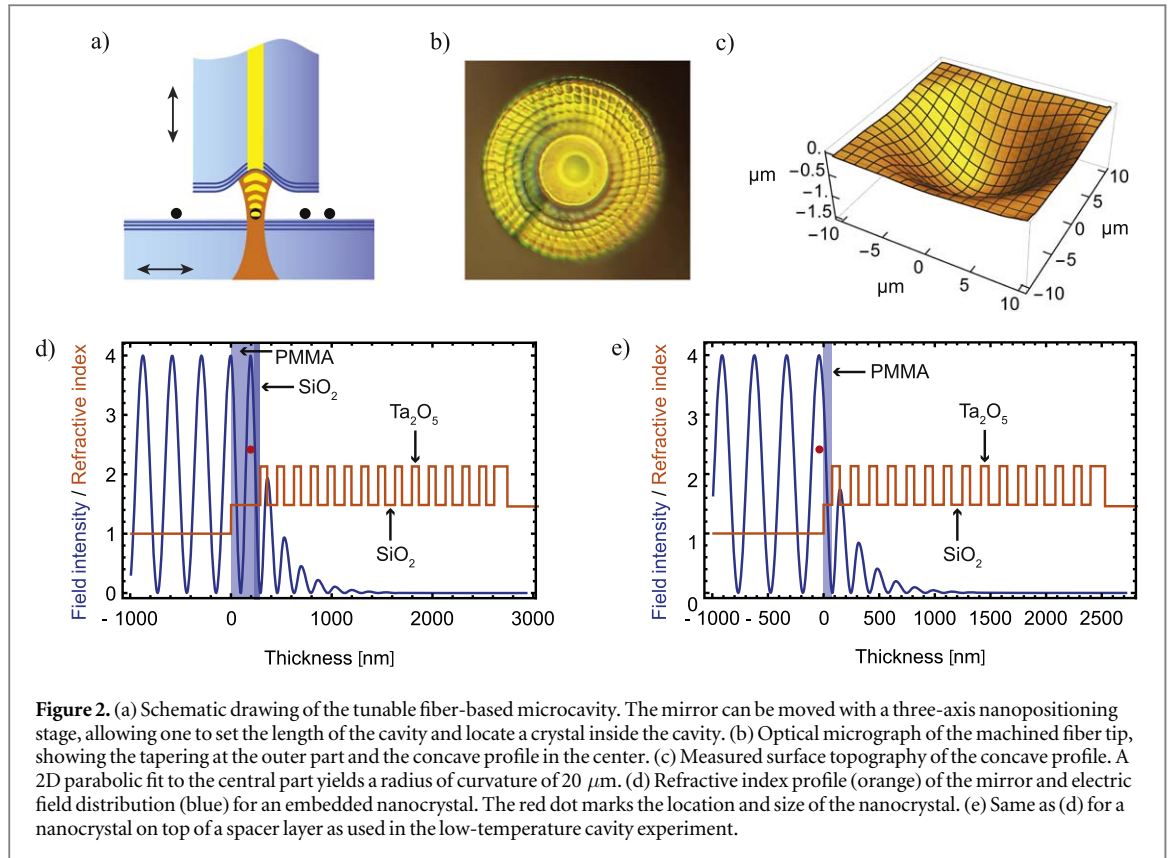
$$\alpha = 3\epsilon_0 V \frac{n^2 - n_m^2}{n^2 + 2n_m^2} \quad (3)$$

with n and n_m the refractive indices of the crystal and surrounding medium, ϵ_0 the vacuum dielectric constant, and $V = 4/3\pi r^3$ the volume of the crystal. It is apparent that particles embedded in a dielectric layer lead to a reduced scattering loss. For the case of Y_2O_3 particles ($n = 1.93$) embedded in a PMMA layer ($n_m = 1.49$), the calculation above yields a reduction of B by a factor of 6.7 compared to a crystal in air.

Furthermore, the presence of the nanocrystal and the surrounding dielectric sensitively influence the excited state lifetime of atomic dipoles inside, and thereby affect the light–matter coupling strength. For a nanocrystal far in the Rayleigh regime (diameter $\lesssim 20 \text{ nm}$) embedded in a medium, the lifetime is given by [29–32]

$$\tau(x) = \tau_0 n_r(x) \left(\frac{n_r(x)^2 + 2}{3} \right)^2, \quad (4)$$

where τ_0 is the lifetime in bulk Y_2O_3 and $n_r(x) = n/(x + (1-x)n_m)$ is the relative refractive index with the effective surrounding refractive index $x + (1-x)n_m$ described by the medium refractive index n_m and the filling factor x [32]. The latter takes into account partially surrounding media, as is the case e.g. for a nanocrystal



on a glass substrate. The resulting prolonged lifetime for small crystals is due to the boundary condition of the crystal–air interface, which makes the crystal act as an off-resonant cavity that suppresses the local field inside. According to equation (4), ions in small Y_2O_3 nanocrystals in air should show a lifetime $\tau_{\text{air}} = \tau(0) = 7.0\tau_0$. For larger crystals, calculations [30, 32] and measurements [31, 32] show that τ decreases with size, and the presence of a surrounding dielectric further reduces τ .

To estimate the effect of embedding, the calculations referred to above are not adequate for our situation, since we do not embed into a bulk medium but into a thin film on a mirror. We therefore perform finite difference time domain simulations (Lumerical) and analyze the spontaneous emission of a dipole located in a $80\ \text{nm}$ cube of Y_2O_3 on a Bragg mirror with embedding, see figure 2(d). We find that the emission rate increases by up to a factor of 3.8 as compared to the dipole in a crystal in free space. This shows that embedding increases the local field strength within the crystal, and it will in the same way increase the coupling strength to the cavity field.

We experimentally study these effects for our sample. Figure 1(e) shows fluorescence lifetime measurements as function of the count rate for crystals prepared in two different ways. First, the particles are spin-coated onto a fused silica substrate to serve as a reference. Second, we embed the particles into a PMMA layer on top of a dielectric mirror (see figure 2(d)). To ensure that the nanoparticle resides in a field maximum of the standing wave that will be formed in a cavity, a three-step preparation was used: first, a layer of $55\ \text{nm}$ of SiO_2 was applied to the mirror by electron beam evaporation. Then, nanocrystals are deposited on this layer and are thus centered on an electric field maximum. Third, a $235\ \text{nm}$ thick layer of PMMA is spin-coated to cover the particles. The total optical thickness of the two layers of comparable refractive index $n_m = \{1.46, 1.49\}$ is $(3/4)\lambda/n_m$ for the transition wavelength $\lambda = 580\ \text{nm}$. For this thickness, a simulation of the electric field inside the layer [33] shows that it is as large as in the vacuum part of the cavity, thereby maximizing light–matter coupling (see figure 2(d)).

In the experiment, we observe the expected correlation between lifetime and count rate for both samples, when again assuming the relation between count rate and crystal size as discussed above. The solid line shown in figure 1(e) agrees with the measurement and is a fit to a prediction of the size-dependent lifetime of a dipole in the center of a dielectric sphere [30],

$$\tau(r, x) = \tau_0 n_r(x) U(r), \quad (5)$$

with $U(r)$ as given in equation (28) in [30]. Assuming a single central dipole reasonably approximates the continuous ion distribution in the nanocrystals as long as $r < \lambda/(2\pi n) \approx 50\ \text{nm}$. We use the filling factor x as a

fit parameter and obtain best agreement for $x = 0.30$. This value is smaller than expected, such that other factors that reduce the lifetime in addition to the presence of the substrate cannot be excluded.

We can also observe the effect of embedding the crystals in a thin film, which leads to a marked reduction of the lifetime in the measurement [34]. The right panel of figure 1(e) shows the lifetime for the two cases averaged over all crystals, and we observe an averaged lifetime reduction by a factor of 1.5 for the embedded sample, which features a lifetime of $\tau_{\text{emb}} = (1.26 \pm 0.03)$ ms as compared to $\tau_{\text{sub}} = (1.91 \pm 0.06)$ ms for the sample on silica. The observed average lifetime reduction is in agreement with the FDTD simulation when considering that the simulation compares a crystal in free space with an embedded one, while the measurement compares crystals on a substrate with embedded ones. If we rely on the model used for the fit of the lifetime data, we can use the ratio $\tau_{\text{air}}/\tau(0) = 2.5$ to calculate the expected lifetime in air for the measured data. With this, we obtain an overall lifetime reduction compared to a crystal in air of $(\tau_{\text{air}}/\tau(0.3)) \times (\tau_{\text{sub}}/\tau_{\text{emb}}) = 3.75$, close to the FDTD prediction.

3. Cavity properties

The main goal of our work is to achieve cavity enhancement of the fluorescence to obtain efficient access to small ensembles and finally individual ions. To realize such a setting, we have developed a fully tunable, cryogenic-compatible Fabry–Perot microcavity as schematically shown in figure 2(a). The setup allows us to locate suitable nanocrystals inside the cavity, and to set the mirror separation to a particular longitudinal mode order to achieve resonance conditions with the ions. The microcavity consists of a macroscopic planar mirror and a concave micro mirror at the end facet of a single-mode optical fiber. The micro mirror is fabricated by CO₂-laser machining [35], where we produce a concave profile with a radius of curvature of 20 μm and depth of 1.5 μm . The fiber tip is furthermore shaped into a conical tip to reduce the tip diameter to ~ 35 μm , which enables a smallest mirror separation of $d = 2$ μm , see figures 2(b), (c). The fiber and the planar mirror are then coated to have a transmission T of 100 ppm at 580 nm as specified and measured by the coating manufacturer. The fiber is mounted on a shear piezoelectric actuator for cavity length stabilization, while the large mirror is mounted on a commercial closed-loop three-axis attocube nanopositioning stage.

The finesse of the cavity is measured to be $\mathcal{F} = 17\,000$ with a variation of 5000 depending on the particular fundamental longitudinal mode, values which are in agreement with simulation and calculations, see below. The variation of the finesse originates from mode mixing between the fundamental and higher order modes due to the non-spherical shape of the concave structure [36]. From the finesse measurement and the known mirror transmission, we can deduce the residual scattering and absorption losses L of the mirrors and obtain a value $L = 30$ ppm.

When the cavity is tuned on resonance, a Purcell factor of $C = 1000\zeta$ is expected for a cavity with a length of 2 μm , which for $\zeta = 1$ quantifies the enhancement of fluorescence of a particular transition. The coherent ${}^5D_0\text{--}{}^7F_0$ can thus be significantly enhanced, however due to its small branching ratio $\zeta_{F_0} \approx 1/60$, the lifetime change is correspondingly smaller, and a Purcell factor $C = 17$ is expected. In the experiments described here, we were not yet able to stabilize the cavity on resonance in the cryostat, and we investigate an alternative approach, which is less sensitive to the cavity resonance condition. We use the ${}^5D_0\text{--}{}^7F_0$ transition for excitation and the ${}^5D_0\text{--}{}^7F_2$ transition for emission, both being simultaneously resonant with the cavity. More detail is given below. This scheme provides high scattering rates also without optimal Purcell enhancement, and reduced background due to the wavelength separation of excitation and detection.

4. Cavity-enhanced spectroscopy

To perform low-temperature spectroscopy, we introduce a mirror carrying nanocrystals in the cavity and cool it down to 8 K. Since the experiments were performed in parallel with the nanocrystal studies described above, an earlier version of sample preparation was used. Here, the particles are not embedded within PMMA but reside on top of a PMMA spacer layer, whose thickness is chosen to locate the nanocrystals in an electric field maximum of the cavity modes, see figure 2(e). To spatially locate a well-isolated crystal of suitable size within the cavity mode, we measure the scattering loss signal of nanocrystals by scanning cavity microscopy [37]. We evaluate the cavity transmission T_c at 580 nm, which is given by

$$T_c = \frac{4T_1T_2}{(T_1 + T_2 + 2L + 2B)^2}, \quad (6)$$

where B accounts for the additional scattering loss introduced by the crystal, $T_1 = 100$ ppm is the fiber mirror transmission, $T_2 = 190$ ppm the planar mirror transmission, which is increased due to the spacer layer, and $L = 30$ ppm the average mirror loss. We calculate T_2 from a transfer matrix model [33] that also reproduces T_1 ,

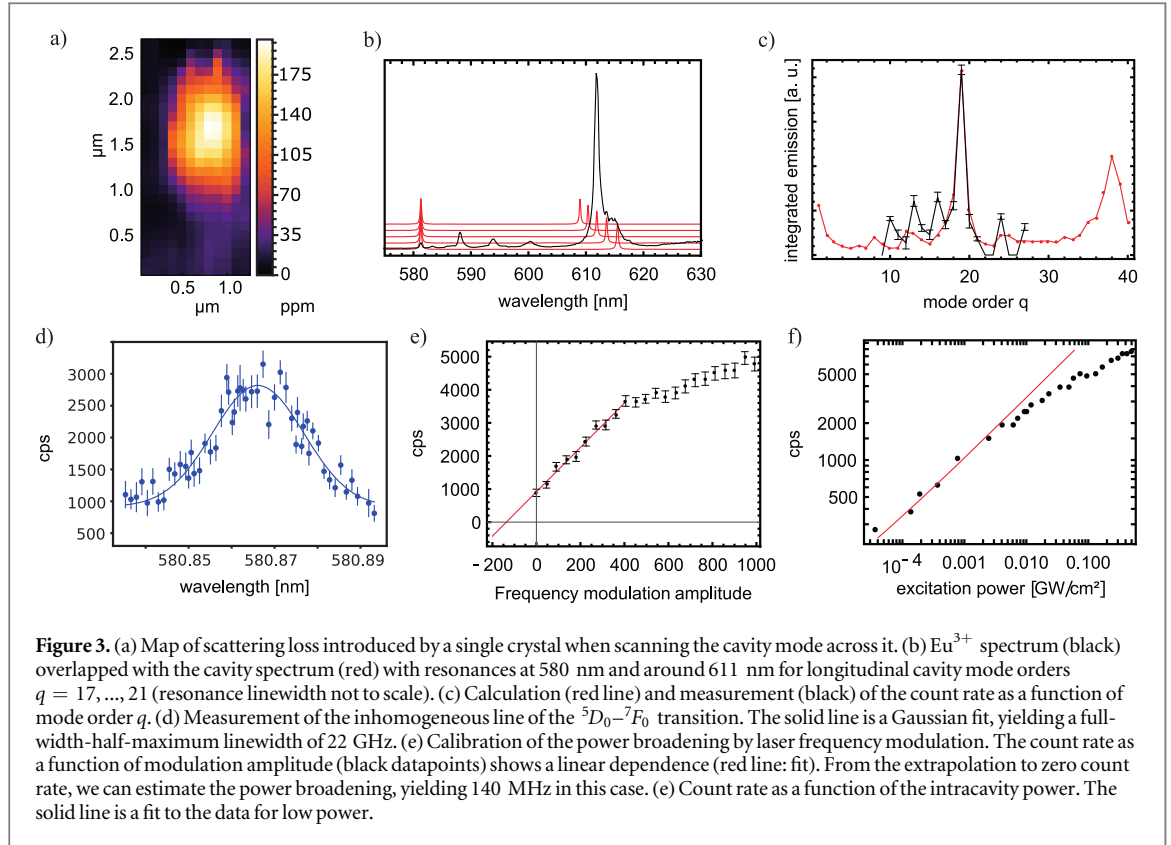


Figure 3. (a) Map of scattering loss introduced by a single crystal when scanning the cavity mode across it. (b) Eu³⁺ spectrum (black) overlapped with the cavity spectrum (red) with resonances at 580 nm and around 611 nm for longitudinal cavity mode orders $q = 17, \dots, 21$ (resonance linewidth not to scale). (c) Calculation (red line) and measurement (black) of the count rate as a function of mode order q . (d) Measurement of the inhomogeneous line of the ⁵D₀-⁷F₀ transition. The solid line is a Gaussian fit, yielding a full-width-half-maximum linewidth of 22 GHz. (e) Calibration of the power broadening by laser frequency modulation. The count rate as a function of modulation amplitude (black datapoints) shows a linear dependence (red line: fit). From the extrapolation to zero count rate, we can estimate the power broadening, yielding 140 MHz in this case. (e) Count rate as a function of the intracavity power. The solid line is a fit to the data for low power.

and find L from the empty cavity finesse measurement. From the uncertainty of the finesse measurement we find an uncertainty for T_p , L of $< 10\%$, and a similar value for B . From the scattering loss B (equation (1)) and the mode waist w_0 we calculate the scattering cross section σ and the volume of the crystal $V = 4/3\pi r^3$ with radius r .

We select crystals that are large enough to provide a suitable ion ensemble for fluorescence measurements, but small enough to maintain the outcoupling efficiency of the fluorescence light from the cavity

$$\eta = \frac{T_2}{T_1 + T_2 + 2L + 2B} \quad (7)$$

at a high level. Figure 3(a) shows the scattering loss of a single crystal when scanning the cavity mode across it at a cavity length $d = 5.5 \mu\text{m}$. The shape represents the cavity mode, while the asymmetry is due to a miscalibration of the nanopositioning stage at short length scales. From the peak loss $B = 203 \pm 20$ ppm observed for perfect spatial alignment, for which $\eta = 0.26$, we can calculate the crystal size and obtain a value of $2r = 91 \pm 3$ nm. Together with the doping concentration of 0.5%, this allows us to estimate the number of ions contained in the crystal, yielding $N = 3 \times 10^4$ ions in this case.

To obtain a fluorescence signal from the cavity, we take advantage of the dominant emission of the ⁵D₀-⁷F₂ transition at 611 nm, which provides larger signals also for an unstabilized cavity. We excite the ⁵D₀-⁷F₀ transition at 580 nm and couple the emission of the ⁵D₀-⁷F₂ transition to the cavity. This detection scheme requires having the cavity resonant with both the excitation light at 580 nm and the emission light at 611 nm. Figure 3(b) shows the principle of the scheme, where the Eu³⁺ spectrum is overlapped with the cavity resonances at 580 and 611 nm, where at the former wavelength, the longitudinal cavity mode order is varied from $q = 17, \dots, 21$. For $q = 19$, both 580 and 611 nm light are resonant. Figure 3(c) shows a calculation and a measurement of the count rate as a function of mode order q for 580 nm cavity excitation. To perform the measurement, the cavity length was tuned to a particular mode order q , and modulated around the set value with an amplitude close to 4 nm, which is more than 250 cavity linewidths $\kappa = \frac{c}{2(q\lambda/2)\mathcal{F}} \approx 1.3$ GHz at 580 nm, with a rate of 10 Hz. We use a single photon counter to collect the fluorescence light from the cavity, and we perform time resolved counting synchronized with the modulation. We make a histogram of the detected counts with a bin size corresponding to about 2κ , and evaluate the averaged peak count rate per bin after several seconds of data acquisition.

Next, we perform spectroscopy of the ⁵D₀-⁷F₀ transition. We set the cavity length to $q = 19$ and measure the count rate as describe above as a function of the laser wavelength across the range of the inhomogeneous line of the ⁵D₀-⁷F₀ transition. Figure 3(d) shows the obtained spectrum. We fit it with a Gaussian profile and find a FWHM linewidth of 22 GHz, which agrees very well with the linewidth in bulk samples at this doping

concentration, and thereby confirms the high crystal quality [38]. We note that this represents the first low-temperature spectroscopy of a single $\text{Eu}^{3+}:\text{Y}_2\text{O}_3$ nanocrystal of such a small size.

To understand the origin of the observed spectrum, we estimate the number of ions in the crystal within the frequency interval of the homogeneous linewidth of a single ion. We assume a Gaussian spectral ion density and neglect the hyperfine structure. With $N \approx 3 \times 10^4$ ions in the crystal with an expected homogeneous linewidth of about $\gamma_h = 200$ kHz at 10 K [24] spread over an inhomogeneous linewidth of $\gamma_{inh} = 22$ GHz. This estimate leads to a peak density $n = 2\sqrt{\ln(2)}/\pi N\gamma_h/\gamma_{inh} = 0.27$, i.e. the ion transitions are spaced by about four linewidths, and low power spectroscopy would in most cases address no or at most a single ion.

To obtain the observed signal, we use a very high excitation intensity (several GW cm^{-2}), which leads to strong power broadening, and thus off-resonant excitation of small ion ensembles. To calibrate the amount of power broadening, we modulate the frequency of the excitation laser and measure the count rate as a function of the modulation amplitude (figure 3(e)). We observe a linear signal increase up to an amplitude that approximately corresponds to the cavity linewidth. From an extrapolation of the linear dependence to zero count rate, we can estimate the power broadening. For the measurement shown, this amounts to 140 MHz, taken at an intracavity power of ~ 53 mW and an intensity of ~ 3.5 GW cm^{-2} .

We furthermore measure the count rate on resonance (without frequency modulation) as a function of the excitation power. The scattering rate of a two-level system is given by $R_{sc} = \frac{\gamma}{2} \frac{S_0}{1 + S_0 + (2\Delta/\gamma)^2}$, and the power-broadened linewidth scales with $\sqrt{S_0} = \Omega\sqrt{2}/\gamma$, where S_0 is the saturation parameter, Ω the Rabi frequency, and γ the excited state decay rate. Figure 3(f) shows a measurement of the count rate as function of the excitation power. The observed power dependence follows the expected $\sqrt{S_0}$ relation over a large range (red solid line). For the weakest accessible excitation power of 0.15 mW, where we still have a significant signal to background ratio of 2, the excitation is a factor 400 weaker than for the value used for the calibration, such that the broadening is a factor 20 smaller, i.e. ~ 7 MHz. With an average spectral ion separation of $\delta = 750$ kHz, this corresponds to probing ~ 10 ions. At this power level, we measure $R_{det} = 300$ counts s^{-1} on resonance, such that the single ion count rate is approximately 30 counts s^{-1} . This value is already larger than the estimated single ion count rate for confocal detection, despite the fact that we collect only a single transition.

We can obtain an order of magnitude estimate of the achieved effective Purcell factor C by comparing the total measured count rate with the expected free space scattering rate after estimating the collection and detection efficiencies and integrating over the power-broadened distribution. The emission rate in the cavity R_c can be calculated from the inferred total count rate R_{det} by $R_c = R_{det}/(\eta\eta_{det}) = 11\,000$ s^{-1} , where $\eta_{det} = 0.1$ includes the detector quantum efficiency, the loss on the optical path, and the cavity outcoupling efficiency $\eta = 0.25$. Compared to the integrated free space scattering rate for the ensemble under the inferred power broadening, $R_{sc} = \int \gamma/2(S_0/\delta)1/(1 + S_0 + (2\Delta/\gamma)^2)d\Delta = 5200$ s^{-1} with $\gamma = 770$ Hz the measured decay rate and $S_0 = 93$ MHz, we obtain $C = R_c/R_{sc} \sim 2$. This shows a net improvement of the signal due to the cavity.

We can compare the observed value with an estimate of the theoretically achievable Purcell factor for this configuration. At the transition wavelength of 611 nm, the cavity finesse amounts to $F = 5000$, and for the double resonance condition at $q = 19$, the mode volume amounts to $35\lambda^3$, such that $C_{F_2} = 210\zeta_{F_2} \approx 80$ for a branching ratio into the particular crystal field level $\zeta_{F_2} \approx 0.4$ as inferred from the spectrum. The linewidth of the ${}^5D_0-{}^7F_2$ transition is inferred from spectroscopy on a powder and estimated to be $\gamma_{h,F_2} > 200$ GHz. This is larger than the cavity linewidth $\kappa = 1.3$ GHz and reduces the achievable Purcell factor to $C_{eff,F_2} = C_{F_2}\kappa/\gamma_{h,F_2} = 2.5$, in agreement with the measured value.

5. Conclusion

We have performed cavity-enhanced spectroscopy measurements of ensembles of a few Eu^{3+} ions in an isolated nanocrystal. We characterized the crystal size, such that an estimation of important parameters such as the number of ions probed and the single ion count rate was possible. From an order of magnitude estimate, we infer an effective Purcell factor $C \sim 2$, evidencing the benefit of cavity enhancement. We have also shown that embedding the crystals in a thin film leads to an additional reduction of the lifetime, and calculations show a significant reduction of scattering loss.

A much larger enhancement is expected for an actively stabilized cavity which is continuously coupled to the ${}^5D_0-{}^7F_0$ transition for both excitation and detection. We are currently developing a custom-built nanopositioning stage with significantly improved passive stability, which has recently enabled us to stabilize the cavity on resonance during the entire cooling cycle of the cryostat, giving good prospects for future experiments. For a realistic cavity with $\mathcal{F} = 10^5$ and $d = 2$ μm , $C_{F_0} = 100$ is expected, such that up to 10^5 photons s^{-1} can be scattered into the cavity, enabling efficient single ion readout. This can open the way to address several individual Eu ions as a multi-qubit register with promising coherence properties. We are also exploring different materials

including $\text{Er}^{3+}:\text{Y}_2\text{O}_3$, which has a narrow optical transition in the telecom band, ideal for long distance quantum communication applications.

Acknowledgments

We acknowledge support from T Bagci and Q Unterreithmeier during early phases of the experiment. This work was partially funded by the European Union H2020 research and innovation programme under grant agreement No. 712721 (NanoQTech), and the DFG Cluster of Excellence Nanosystems Initiative Munich. TWH acknowledges funding from the Max-Planck Foundation, BC acknowledges financial support from the Cellex ICFO-MPQ postdoctoral fellowship programme. ICFO is also supported by MINECO Severo Ochoa through grant SEV-2015-0522, by fundació Cellex, by CERCA Programme/Generalitat de Catalunya, and from the Spanish Ministerio de Economía y Competitividad (MINECO, FIS2016-81696-ERC).

ORCID iDs

Bernardo Casabone  <https://orcid.org/0000-0002-3695-7539>

Hugues de Riedmatten  <https://orcid.org/0000-0002-4418-0723>

David Hunger  <https://orcid.org/0000-0001-6156-6145>

References

- [1] Goldner P, Ferrier A and Guillot-Noël O 2015 Rare earth-doped crystals for quantum information processing *Handbook on the Physics and Chemistry of Rare Earths* ed J-C G Bünzli and V K Pecharsky vol 46 (Amsterdam: Elsevier) pp 1–78
- [2] Zhong M, Hedges M P, Ahlefeldt R L, Bartholomew J G, Beavan S E, Wittig S M, Longdell J J and Sellars M J 2015 *Nature* **517** 177
- [3] Kolesov R, Xia K, Reuter R, Jamali M, Stöhr R, Inal T, Siyushev P and Wrachtrup J 2013 *Phys. Rev. Lett.* **111** 120502
- [4] Laplane C, Jobez P, Etesse J, Timoney N, Gisin N and Afzelius M 2015 *New J. Phys.* **18** 013006
- [5] Gündoğan M, Ledingham P M, Kutluer K, Mazzera M and de Riedmatten H 2015 *Phys. Rev. Lett.* **114** 230501
- [6] Böttger T, Thiel C, Cone R and Sun Y 2009 *Phys. Rev. B* **79** 115104
- [7] Ohlsson N, Mohan R K and Kröll S 2002 *Opt. Commun.* **201** 71
- [8] Longdell J, Sellars M and Manson N 2004 *Phys. Rev. Lett.* **93** 130503
- [9] Kolesov R, Xia K, Reuter R, Stöhr R, Zappe A, Meijer J, Hemmer P and Wrachtrup J 2012 *Nat. Commun.* **3** 1029
- [10] Utikal T, Eichhammer E, Petersen L, Renn A, Göttinger S and Sandoghdar V 2014 *Nat. Commun.* **5** 3627
- [11] Nakamura I, Yoshihiro T, Inagawa H, Fujiyoshi S and Matsushita M 2014 *Sci. Rep.* **4** 7364
- [12] Siyushev P et al 2014 *Nat. Commun.* **5** 3895
- [13] Dibos A M, Raha M, Phenicie C M and Thompson J D 2018 *Phys. Rev. Lett.* **120** 243601
- [14] Zhong T et al 2018 arXiv:1803.07520
- [15] Chou C W et al 2005 *Nature* **438** 828
- [16] Bernien H et al 2013 *Nature* **497** 86
- [17] Stockill R et al 2017 *Phys. Rev. Lett.* **119** 010503
- [18] Zukowski M, Zeilinger A, Horne M A and Ekert A K 1993 *Phys. Rev. Lett.* **71** 4287
- [19] Pan J-W, Bouwmeester D, Weinfurter H and Zeilinger A 1998 *Phys. Rev. Lett.* **80** 3891
- [20] Olmschenk S, Matsukevich D, Maunz P, Hayes D, Duan L-M and Monroe C 2009 *Science* **323** 486
- [21] Hunger D, Steinmetz T, Colombe Y, Deutsch C, Hänsch T W and Reichel J 2010 *New J. Phys.* **12** 065038
- [22] Benedikter J, Kaupp H, Hümmer T, Liang Y, Bommer A, Becher C, Krueger A, Smith J M, Hänsch T W and Hunger D 2017 *Phys. Rev. Appl.* **7** 024031
- [23] Perrot A, Goldner P, Giaume D, Lovrić M, Andriamiadamanana C, Gonçalves R and Ferrier A 2013 *Phys. Rev. Lett.* **111** 203601
- [24] Bartholomew J G, de Oliveira Lima K, Ferrier A and Goldner P 2017 *Nano Lett.* **17** 778
- [25] Serrano D, Karlsson J, Fossati A, Ferrier A and Goldner P 2018 *Nat. Commun.* **9** 2127
- [26] Lauritzen B, Timoney N, Gisin N, Afzelius M, de Riedmatten H, Sun Y, Macfarlane R and Cone R 2012 *Phys. Rev. B* **85** 115111
- [27] de Oliveira Lima K, Gonçalves R R, Giaume D, Ferrier A and Goldner P 2015 *J. Lumin.* **168** 276
- [28] Wind M, Vlieger J and Bedeaux D 1987 *Physica A* **141** 33
- [29] Chew H 1988 *Phys. Rev. A* **38** 3410
- [30] Le Kien F, Quang N H and Hakuta K 2000 *Opt. Commun.* **178** 151
- [31] Schniepp H and Sandoghdar V 2002 *Phys. Rev. Lett.* **89** 257403
- [32] Duan C-K, Reid M F and Wang Z 2005 *Phys. Lett. A* **343** 474
- [33] Furman S A and Tikhonravov A 1992 *Basics of Optics of Multilayer Systems* (Paris: Atlantica Séguier Frontières)
- [34] Khalid A, Chung K, Rajasekharan R, Lau D W, Karle T J, Gibson B C and Tomljenovic-Hanic S 2015 *Sci. Rep.* **5** 11179
- [35] Hunger D, Deutsch C, Barbour R J, Warburton R J and Reichel J 2012 *AIP Adv.* **2** 012119
- [36] Benedikter J, Hümmer T, Mader M, Schlederer B, Reichel J, Hänsch T W and Hunger D 2015 *New J. Phys.* **17** 053051
- [37] Mader M, Reichel J, Hänsch T W and Hunger D 2015 *Nat. Commun.* **6** 7249
- [38] Kunkel N, Ferrier A, Thiel C W, Ramirez M O, Bausa L E, Cone R L, Ikesue A and Goldner P 2015 *APL Mater.* **3** 096103